Journal of Nuclear Materials 558 (2022) 153363

Contents lists available at ScienceDirect

Journal of Nuclear Materials

journal homepage: www.elsevier.com/locate/jnucmat

Predicting the hydride rim by improving the solubility limits in the Hydride Nucleation-Growth-Dissolution (HNGD) model.

Florian Passelaigue[a,*], Pierre-Clément A. Simon[a,b], Arthur T. Motta[a]

[a] Ken and Mary Alice Lindquist Department of Nuclear Engineering, The Pennsylvania State University, University Park, PA 16802 US
[b] Idaho National Laboratory, Computational Mechanics and Materials Department, 1955 Fremont Ave., Idaho Falls, ID 83415, US

ARTICLE INFO

Article history:
Received 27 July 2021
Revised 13 October 2021
Accepted 20 October 2021
Available online 22 October 2021

Keywords:
Nuclear material
Zircaloy
Zirconium hydride
HNGD
Bison

ABSTRACT

During operation of a light water reactor, waterside corrosion of the Zircaloy nuclear fuel cladding causes hydrogen pickup. The absorbed hydrogen can redistribute in the cladding driven by existing concentration, stress, and temperature gradients. When the concentration reaches the solubility limit, hydrides precipitate. These hydrides can be more brittle than the Zircaloy matrix, so they can endanger the cladding integrity during a transient if their concentration is too high. In recent years, extensive efforts have been made to understand hydrogen behavior and to develop simulation tools able to predict hydrogen diffusion and hydride precipitation and dissolution. These efforts led to the development of the Hydride Nucleation-Growth-Dissolution (HNGD) model and its implementation into the nuclear fuel performance code Bison. While it offers a significant improvement and accurately predicts the amount of precipitates, this model fails to predict the thickness of the hydride rim under a temperature gradient. The current work presents the limitation of the HNGD model and proposes two hypotheses to improve the model's accuracy. The first hypothesis introduces a time dependency to the supersolubility to reduce the nucleation barrier as hydrogen atoms find more favorable nucleation sites. The second one introduces a hydride content dependency to the solubility. These hypotheses were validated and implemented into Bison and are now available to the user community. The modified HNGD model accurately predicts the hydride rim thickness, and it was demonstrated that this updated model can be used in Bison to model Zircaloy cladding with a zirconium inner liner. Finally, potential experimental and numerical methods are discussed to further validate these hypotheses.

Published by Elsevier B.V.

1. Introduction

During the operation of a light water reactor, the Zircaloy nuclear fuel cladding undergoes waterside corrosion and picks up hydrogen as a result [1]. The absorbed hydrogen redistributes within the cladding following any temperature, concentration, and stress gradients present. When the local concentration of hydrogen exceeds the solubility limit, zirconium hydrides precipitate [2,3]. The hydride phase is more brittle than the Zircaloy matrix, so a high number of hydrides particles can decrease the ductility of the cladding material and thus compromise its integrity in case of an accident.

This is why a simulation tool able to predict the redistribution of hydrogen and the formation of hydrides is paramount to safely extend the life of nuclear fuel. Work performed by Lacroix et al. on hydrogen behavior and hydride precipitation and dissolution ([2,3]), resulted in the Hydride Nucleation Growth Dissolution (HNGD) model, which allows a more precise calculation of hydrogen distribution between phases. This model was implemented in the finite element based nuclear fuel performance code Bison, developed at Idaho National Laboratory (INL) [4]. This code is based on the finite element framework MOOSE, also developed at INL. Bison can be used to model different types of nuclear fuel, including LWR fuel rods and TRISO particle fuel. It is able to couple numerous physical phenomena, including mechanical (elastic and plastic deformation, mechanical contact, fracture, ...), thermal (heat diffusion, gap heat transfer, ...), and irradiation-based (creep, swelling, densification, fission gas production, ...) [5].

1.1. HNGD Model

There are two variables of interest calculated in the HNGD model: the concentration of hydrogen in solid solution C_{ss} and in hydrides C_{Prec}, both given in wt.ppm. The total local hydrogen con-

* Corresponding author.
E-mail address: fpp8@psu.edu (F. Passelaigue).

https://doi.org/10.1016/j.jnucmat.2021.153363
0022-3115/Published by Elsevier B.V.

centration is given by their sum

$$C_{tot} = C_{ss} + C_{Prec}. \quad (1)$$

The evolution of the hydrogen concentrations is governed by:

$$\begin{cases} \frac{\partial C_{ss}}{\partial t} = -\nabla J - S \\ \frac{\partial C_{Prec}}{\partial t} = S \end{cases}, \quad (2)$$

where S is the hydride source term (that is, the flux of hydrogen towards hydride particles, occurring through either nucleation of new hydrides or the growth of existing ones) and J is the hydrogen flux, defined as:

$$J = -D\nabla C_{ss} - \frac{DQ^* C_{ss}}{RT^2}\nabla T, \quad (3)$$

with $T[K]$ the temperature, $D[m^2/s]$ the diffusion coefficient of hydrogen in zirconium (following an Arrhenius law), and $Q^*[J/mol]$ the heat of transport of hydrogen in zirconium (constant). Thus the hydrogen flux expressed in Eq. 3 accounts for both Fickian and Soret diffusion. The effect of stress on hydrogen diffusion, however, is not included in the model. The source term for hydride precipitation S depends on the local conditions of concentration and temperature [2,3]. Hydride dissolution occurs below the solubility limit (also known as Terminal Solid Solubility for Dissolution TSS_D), hydride nucleation occurs above the supersolubility limit (also known as Terminal Solid Solubility for Precipitation TSS_P), and hydride growth occurs anywhere above the solubility if hydrides are present. The difference between the supersolubility and solubility is due to the extra energy required to nucleate new hydrides (interface creation and specific volume difference) [1]. The equations and parameters for these phenomena are detailed in [2,3].

The HNGD model has been shown to accurately predict the hydrogen behavior in the cladding and specifically the partition of hydrogen between hydrides and hydrogen in solid solution in a range of experiments. In particular, it can predict the precipitation and dissolution of hydrides during thermal transients ([2,3]) and the hydrogen profile after an annealing under a temperature gradient of samples that were uniformly loaded with hydrogen ([6]). However, non-physical behaviors arise when (i) the initial hydrogen distribution is nonuniform, for example when the hydrogen loading is created by forming a hydride rim rather than a uniform charging, or (ii) the system reaches steady state. These shortcomings have been revealed by testing the HNGD model against experimental measurements of hydrogen distribution under a temperature profile performed by Kammenzind and published by Merlino in [7] (this M.Eng. paper was made available on the author's Github repository [8]). These are discussed in the following section.

1.2. Kammenzind's experiments [7]

The experiments performed by Kammenzind and summarized by Merlino in [7,8] constitute the base of the validation presented in this work. Two sets of experiments were presented.

1.2.1. Linear cases

In these cases, 2.54 cm-long Zircaloy samples are uniformly loaded with hydrogen using gas charging (from 37 to 468 wt.ppm), and then subjected to a linear temperature profile for 6 to 77 days. A hydride peak forms at the cold interface. These cases were designed to reach steady state by the end of the experiment.

1.2.2. Asymmetrical cases

In these experiments, 3.8 cm-long Zircaloy samples are loaded with hydrogen via electrolysis, forming a rim of solid hydrides at one end of the sample. The sample is subjected to a temperature distribution as shown in Fig. 1 (brown line). Initially, the rest of the sample does not contain a significant amount of hydrogen. The samples are then subjected to an asymmetrical temperature profile for a long time: 95 to 209 days. The right end (where the hydride rim is) is maintained at a higher temperature than the left. The maximum temperature is reached at ≈ 2.5 cm from the cold (left) side. During the annealing, the hydride rim dissolves, emitting hydrogen into the remainder of the sample. This hydrogen migrates towards the cold side, where hydride particles precipitate (red markers in Fig. 1). The goal of these experiments was to create conditions analogous to a LWR core in terms of hydrogen pick-up: the initial hydride rim serves as a hydrogen source. Note that these experiments were not designed to reach steady state.

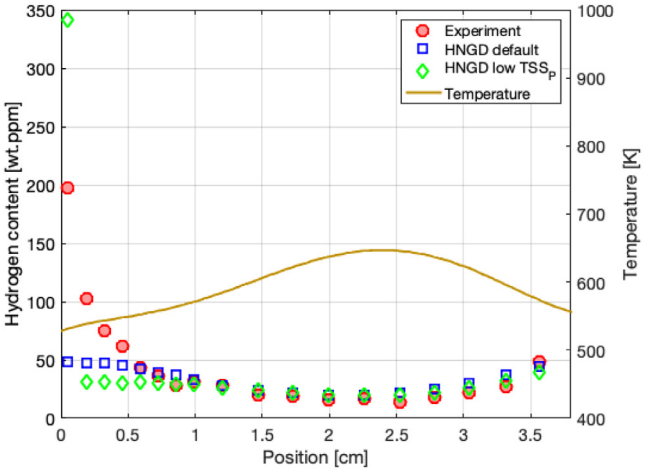

Fig. 1. Kammenzind's asymmetrical case A53[7,8]: comparison of the data (red circles) with a default HNGD simulation (blue squares) and an HNGD simulation using a low supersolubility fit (green diamonds). The model fails to predict the hydride profile on the left of the sample: it either predicts no precipitation at all (default) or precipitation in a single node (low TSS_P). (For interpretation of the references to colour in this figure legend, the reader is referred to the web version of this article.)

1.3. Structure of this paper

The first purpose of this study is to identify the mechanism that causes some of the limitations of the current HNGD model by comparing its predictions against experimental measurements in Section 2. In Section 3, we present two hypotheses that influence the nucleation barrier quantified by the supersolubility (TSS_P), and the equilibrium concentration of hydrogen in solution, quantified by the solubility (TSS_D), to better predict the thickness of the hydride rim. The predictions of the modified HNGD model (shortened as "mHNGD model") are then presented in Section 4, where we validate the updated model against experimental measurements [2,3,6,7]. We also demonstrate the possibility to apply it to Zircaloy cladding containing a zirconium inner liner [9]. Finally, in Section 5 we discuss how to further test these hypotheses.

2. HNGD Model limitations

A key issue with the initial HNGD model is that it predicts an infinitely small hydride rim thickness, that is only limited by the mesh size used in the simulation. Even if an extended hydrided region exists at some point during the simulation, it is reduced to a single mesh node at steady state. This Section details why this issue occurs and how it appears when trying to model the experimental results from [7,8].

2.1. Preliminary: Diffusion-controlled experiments

Sawatzky's and Kammenzind's experiments are diffusion-controlled, as it takes days for the hydrogen to migrate from one end of the sample to the other. Compared to this time scale, even hydride growth (the slowest of the hydride dissolution/precipitation phenomena) is almost instantaneous. So a good approximation is to assume that, if hydride particles are present, the concentration of hydrogen in solid solution is equal to the hydrogen solubility in the material, i.e. there is local equilibrium between the hydrides and the hydrogen in solid solution. This can be written as

$$C_{Prec} > 0 \Rightarrow C_{ss} = TSS_D. \tag{4}$$

2.2. Instability of the hydrided region

We consider the simulation of an experiment is subjected to a temperature gradient for an extended period, in which hydride precipitation is controlled by hydrogen diffusion. If it is assumed that an extended region exists on the cold side in which hydrides are present. This is shown schematically in Fig. 2. In the single-phase region (hotter area, on the right), the hydrogen solubility (dotted line) increases with the temperature, while the concentration of hydrogen in solid solution decreases. In the HNGD model (Fig. 2a), the hydrogen solubility depends only on the temperature, so it decreases continually into the two-phase region. Because this is a diffusion-controlled case, the concentration of hydrogen in solid solution is given by the local solubility. As a result, both the Fick and Soret components of the diffusion flux push hydrogen towards the cold end of the sample. This causes a decrease of hydrogen concentration close to the two-phase / single-phase interface, resulting in the dissolution of hydrides at this location.

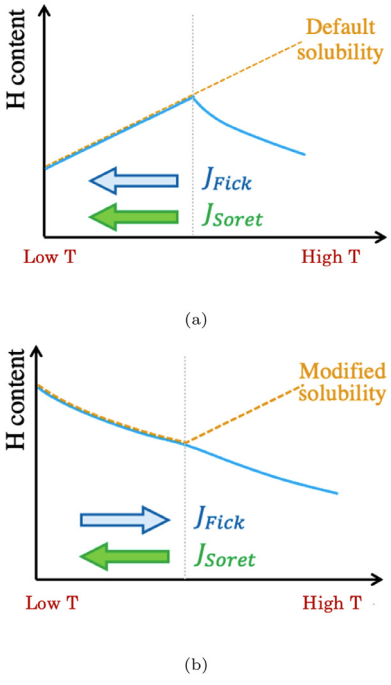

Fig. 2. Schematic of the hydride rim instability issue. We assume the simulation of a sample subjected to a temperature gradient, and with a hydrided region at the cold interface. (a): In the HNGD model, the solubility (TSS_D) only depends on the temperature. As a result, the hydrogen flux resulting from Fick's law and the Soret effect add up and the hydrided region becomes thinner until it is reduced to one node. (b): The hydrided region can exist at steady state only if the two diffusion components compensate each other, which can be obtained by introducing a hydride content dependency to the solubility.

This process then repeats, eventually reducing the hydrided region to a thickness of only one simulation node, which is unphysical. Although this single-node precipitation does not correspond to experiment, this is what happens when trying to model the linear cases described in Section 1.2.1. As a result, an extended hydrided region cannot exist at steady state in the current version of the HNGD model.

For the hydrided region to exist at steady state, the Fick and Soret components of the hydrogen flux have to compensate each other. One way that this can happen is if the hydrogen solubility depends on the hydride content in such a way that it increases close to the interface, as illustrated in Fig. 2.b This concept is fully developed in Section 3.2.

This issue manifests in a slightly different way in the asymmetrical cases described in Section 1.2.2. As shown in Fig. 1, the HNGD model fails to predict any hydride precipitation on the cold side when using the default parameters (blue squares). This is because the concentration of hydrogen in solid solution never reaches the supersolubility limit during the simulation, so no hydride nucleation is triggered. One could argue that the supersolubility fit has significant uncertainties, and that in these particular experiments the TSS_P may be lower than the default HNGD value [2,3] assumed here. However, lowering the supersolubility does not solve this particular issue: Fig. 1 shows that if one uses a significantly lower supersolubility (green diamonds), precipitation does occur, but only in a single simulation node (independently of the mesh size). Again, this behavior is unphysical, so the issue is not resolved by a lower TSS_P, but rather by missing physical considerations.

So, to improve the accuracy of the HNGD model, the update should (i) make hydride nucleation possible on the cold side of the asymmetrical case by modifying the supersolubility limit, and (ii) stabilize the hydride region in both linear and asymmetrical cases by making the solubility limit to be dependent on the local concentration of hydrides.

3. Hypotheses

This section presents two hypotheses developed to address the twin issues of the nucleation trigger and the instability of the hydrided region. While preliminary physical justifications are given below, these two hypotheses were develped based mainly on mathematical observations of the many simulations that were run.

3.1. Supersolubility time dependency

For new hydrides to precipitate, obstacles such as the specific volume difference and formation of a new interface must be overcome, which explains the difference between the hydrogen solubility and its supersolublity [1]: a certain amount of subcooling or an increase in hydrogen content are needed for hydrides to nucleate. However, this description does not account for matrix inhomogeneities (such as dislocations and atomic-scale heterogeneities) that may play a critical role in catalyzing nucleation [10]. To account for these heterogeneities, we assume that during a temperature hold, hydrogen has a higher chance to migrate towards these favorable nucleation spots, resulting in a lower hydride nucleation barrier. We call this nucleation threshold "effective supersolubility", noted TSS_P^{eff}. It replaces the hydrogen supersolubility TSS_P and we represent it mathematically as

$$\begin{cases} \dfrac{\partial T}{\partial t} \neq 0 \Rightarrow TSS_P^{eff} = TSS_P \\ \dfrac{\partial T}{\partial t} = 0 \Rightarrow TSS_P^{eff} = TSS_D + (TSS_P - TSS_D)e^{-\frac{t-t_0}{\tau}} \end{cases} \tag{5}$$

During temperature transients (i.e. $\frac{\partial T}{\partial t} \neq 0$) the effective supersolubility is identical to the supersolubility. During temperature holds

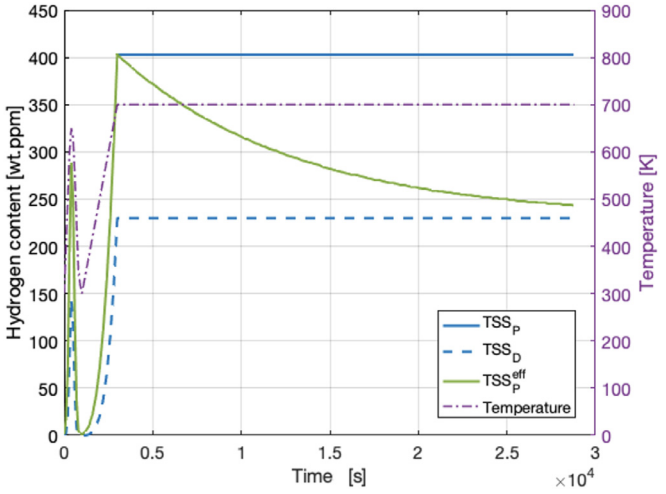

Fig. 3. Illustration of the supersolubility hypothesis with a hypothetical temperature treatment (dot-dash purple). During the thermal transients (0 to 3000s) the TSS_P^{eff} curve (green) follows the default TSS_P (blue). When the annealing starts, the effective supersolubilty decreases exponentially, tending to the solubility TSS_D (dashed blue). (For interpretation of the references to colour in this figure legend, the reader is referred to the web version of this article.)

(i.e. $\frac{\partial T}{\partial t} = 0$) the effective supersolubility decreases exponentially. t_0 is the time when the temperature hold starts, and τ is the time parameter that characterizes the decrease. In this study, we use $\tau = 10^4$ s. This value is chosen so that the modified model is still consistent with the data available. τ is high enough so that it does not impact the simulations of hydride nucleation that are already accurate using the initial HNGD model, in particular in simulating Lacroix's benchmark which was used for the intial development of the HNGD model [2]. In addition, the value of τ is unlikely to be higher than the duration of the experiment; in this case the hypothesis has no impact on the results. This formulation relies on the underlying assumption that the effective supersolubility tends to the solubility value at long holds, and the choice to use the exponential function was made to have the effective supersolubility continuously tend to the solubility without going below. This hypothesis is illustrated in Fig. 3. The purple dot-dash line shows a hypothetical annealing schedule applied to a sample (hydrogen distribution and temperature are uniform in this simulation). The plain and dashed blue lines show the supersolubility and solubility, respectively, and the green line shows the effective supersolubility given by Eq. 5. Effectively, during the temperature transients ($t < 3000$ s) the effective supersolubility follows the TSS_P. When the temperature hold begins, TSS_P^{eff} starts to decrease, tending exponentially to the thermodynamic solubility value TSS_D.

This allows for nucleation to be triggered on the left side of the asymmetrical cases. However, such a modification is not enough to address the second issue outlined in the previous section, as the hydrided region is still unstable.

3.2. Solubility hydride content dependency

A second hypothesis is made on the solubility. We assume that the precipitation of hydrides deforms the matrix so it can accommodate more hydrogen atoms in solution, causing an increase in the effective solubility. Previous work has shown that the elastic strain field affects the distribution of hydrogen around nanoscale hydrides [11]. Other work has shown that dislocations form around hydrides as a result of hydride volume expansion [12]; these dislocations could accommodate additional hydrogen atoms in the matrix. In this work, the impact of this phenomenon on the solubility is mathematically expressed as

$$TSS_D^{eff} = TSS_D + (a\nu_\delta^2 + b\nu_\delta + c) \equiv TSS_D + p(\nu_\delta), \tag{6}$$

where ν_δ is the hydride volume fraction, linked to the hydride content C_{Prec} and local total hydrogen content C_{tot} (Eq. 1) by

$$\nu_\delta = \frac{1}{x_\delta - x_{TSS_D}} \times \frac{C_{Prec}}{C_{tot}\left(1 - \frac{M_H}{M_{Zr}}\right) + 10^6 \frac{M_H}{M_{Zr}}}, \tag{7}$$

with M_H, M_{Zr} the molar masses of hydrogen and zirconium, x_δ the hydrogen atomic fraction at the $\delta/\alpha + \delta$ limit of the $Zr - H$ binary diagram, given in [2,3] by

$$\begin{aligned} x_\delta(T) \approx & -9.93 \times 10^{-11} T^3 + \\ & 8.48 \times 10^{-8} T^2 - 5.73 \times 10^{-5} T + 0.623, \end{aligned} \tag{8}$$

and x_{TSS_D} the solubility expressed as an atomic fraction:

$$x_{TSS_D} = \frac{TSS_D^{eff}}{TSS_D^{eff}\left(1 - \frac{M_H}{M_{Zr}}\right) + 10^6 \frac{M_H}{M_{Zr}}}. \tag{9}$$

The coefficients a, b, c of the polynomial p are determined using the boundary conditions given in the following equation system:

$$\begin{cases} \text{(i) } TSS_D^{eff}(\nu_\delta = 0) = TSS_D \\ \text{(ii) } TSS_D^{eff}(\nu_\delta = 1) = \delta TSS_D \\ \text{(iii) } \dfrac{\partial TSS_D^{eff}}{\partial \nu_\delta}(\nu_\delta = 0) = g \end{cases}. \tag{10}$$

These conditions translate the assumptions that (i) the solubility is unchanged if there is no hydride (ii) the solubility in a solid hydride is a known fraction δ of the unmodified solubility and (iii) the increase in hydrogen solubility caused by the previous precipitation of hydride particles is given by a parameter g. Combining Eqs. 6 and 10 and solving for a, b, c gives the modifying polynomial

$$p(\nu_\delta) = g\nu_\delta - \left((1-\delta)TSS_D + g\right)\nu_\delta^2. \tag{11}$$

Fig. 4 shows the hydride content dependency of the effective solubility TSS_D^{eff} at 600 K using Eqa. 6 and 11. Fig. 4a shows the impact of the parameter g (in wt.ppm in the legend), with a fixed $\delta = 1.05$. g determines the initial slope of the curve, that is, it quantifies the impact of hydride precipitates on the hydrogen solubility at low hydride content. Fig. 4a shows the impact of the parameter δ (no unit) with a fixed $g = 200$ wt.ppm. Fig. 4b shows that δ has a significant influence on the results at very high hydride content, but has little to no impact below 2000 wt.ppm. Thus, while g plays an important role at low hydride contents, δ only has an impact on the model only if there is a hydride rim in the sample. The hydrogen solubility used by the current version of HNGD can be obtained by setting $g = 0$ wt.ppm and $\delta = 1.0$.

It is possible to derive an analytical solution for the steady state hydride distribution predicted by the modified HNGD model. This is done in Appendix A. This analytical solution is useful to verify the implementation of the solubility hypothesis in a code, and it is a powerful tool to determine the optimum values for the parameters g and δ since the linear cases discussed in Section 1.2.2 are at steady state.

4. Results

This Section discusses the results obtained with the modified HNGD (mHNGD) model once it was implemented into Bison.

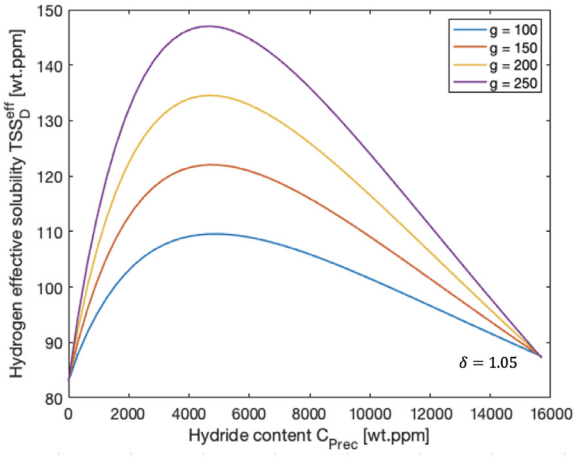

(a)

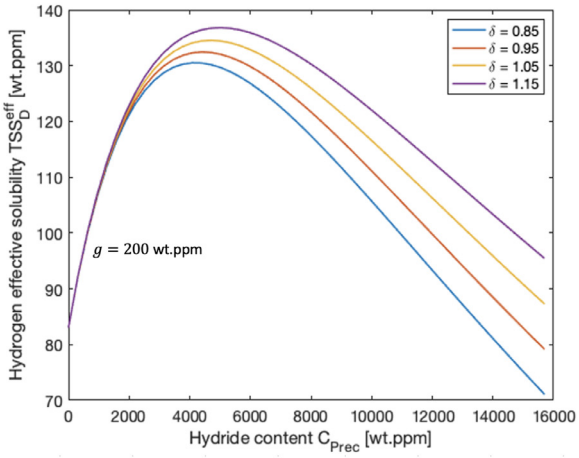

(b)

Fig. 4. The effective solubility (Eq. 6) is plotted at $T = 600$ K as a function of the hydrogen content in hydride particles. (a): the g parameter, in wt.ppm in the legend, quantifies the initial slope. This determines the impact of hydride precipitation on solubility when hydrides start precipitating, making g the most important parameter of this hypothesis. (b): the δ parameter determines the solubility value at high hydride contents, so it impacts the model calculations only if there is a hydride rim in the sample.

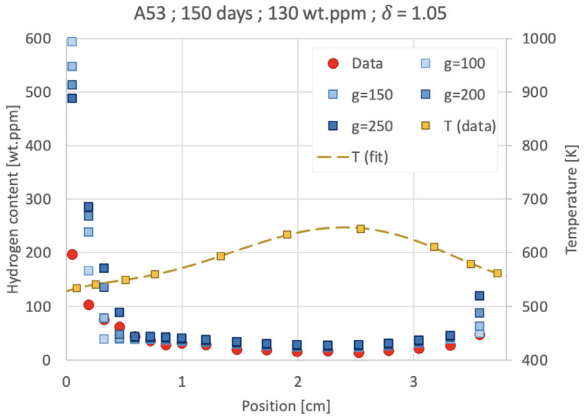

(a)

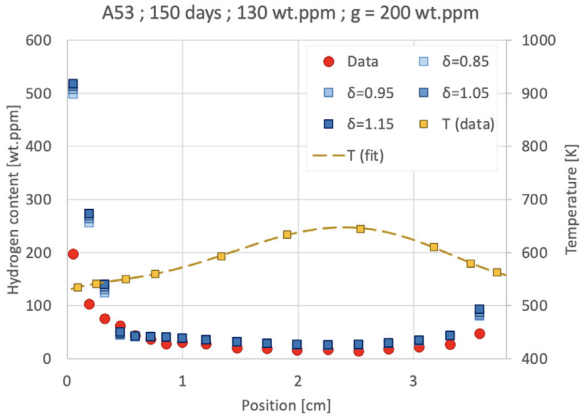

(b)

Fig. 5. Simulation of the Kammenzind asymmetrical cases ([7]) with the mHNGD model: impact of the parameters g and δ. The modified model predicts the formation of a hydrided region on the cold side, which is a significant improvement compared to the HNGD model. The peak height tends to be overestimated, but the predicted thickness of the hydrided region corresponds to the experimental data. (a): the parameter g determines the height and thickness of the hydride peak. A higher g value leads to a thicker peak. (b): the parameter δ impacts how much of the initial hydride rim is dissolved during the annealing, which determines how much hydrogen is released into the rest of the sample.

4.1. Asymmetrical temperature cases

The results for one of the asymmetrical cases discussed in Section 1.2.2 are given in Fig. 5, showing the impact of the parameters g and δ. The mHNGD model predicts the formation of hydrides in more than one node on the left side, which represents a significant improvement compared to the initial HNGD model's predictions shown in Fig. 1. Although the height of the hydride peak is overestimated, the thickness of the hydrided region roughly corresponds to the experimental data (the rightmost point is typically too high to be plotted on the same scale as the other points). Fig. 5a shows that g has the expected impact: the lower its value, the higher and thinner the hydride peak becomes, because the model gets closer to the initial HNGD model (i.e. $g = 0$ wt.ppm). A higher g value causes the hydrided region to be thicker. Fig. 5b shows the effects of δ. It impacts how much of the initial hydride rim is dissolved: a higher value of δ leads to more hydrogen being released into the rest of the sample, causing an increase of hydrogen content in general and of hydride precipitation on the left side. Varying the parameter τ on a wide range (10^4 to 10^7 s) has no significant impact on the simulation of these experiments.

4.2. Compatibility

It is necessary to make sure that the simulations that were accurate with the initial HNGD model are still accurate with the mHNGD model. Fig. 6 plots the data from Lacroix's transients benchmark ([2,3]), along with the calculations of the HNGD and mHNGD models. The simulation results are not affected by the update because (i) the parameter $\tau > 10^4$ s is too high to cause a significant decrease of TSS_P^{eff} during the temperature holds used in the experiment, (ii) the total hydrogen content is 250 wt.ppm, which is too low for the parameter δ to have an impact, and (iii) the variation of solubility due to g is too small to have a significant impact (< 10 wt.ppm).

Fig. 7 shows the impact of the parameters g and τ on the simulations of Sawatzky's experiments. The formation of the hydride peak in these simulations is due to a dissolution-migration-growth cycle that makes the peak shift towards the cold interface while getting higher [4]. As shown in Fig. 7a, the introduction of the parameter g slightly increases the solubility at the hydride peak, making this cycle easier, and resulting in a hydride peak a little lower and more shifted to the left. One can also no-

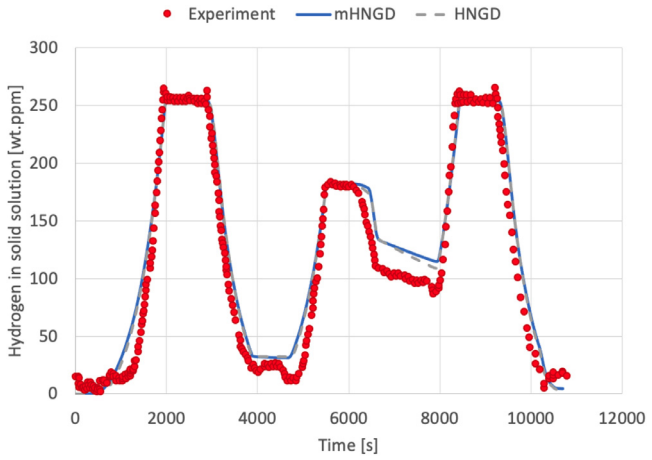

Fig. 6. Compatibility verification: Lacroix's thermal transients [2,3]. Hydrogen in solid solution as a function of temperature during a synchrotron experiment. The results of the simulation are not significantly modified by the introduction of the hypotheses.

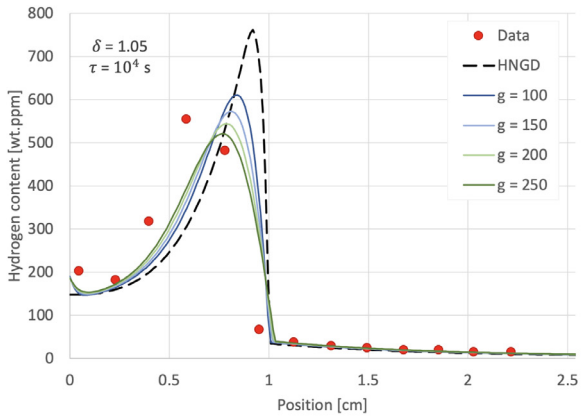

(a)

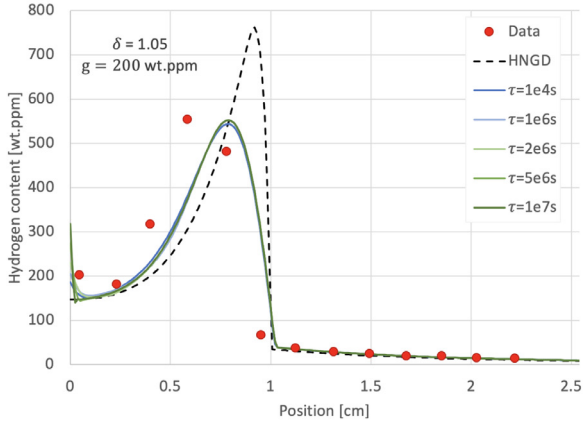

(b)

Fig. 7. Compatibility verification: Sawatzky's experiments [6]. (a): impact of the parameter g on the first experiment. The dissolution/precipitation cycle responsible for the formation of the hydride peak ([4]) is made easier by the increase of solubility at the peak, resulting in a peak that is lower and more shifted to the left. (b): impact of the parameter τ on the second experiment. The simulation depends also on the parameter τ: it has little impact on the results on the range 10^4 to 10^6 s, but at higher values, it impacts the formation of the secondary hydride peak at the cold interface, making it disappear if τ is significantly higher than the duration of the annealing. The parameter δ has no impact.

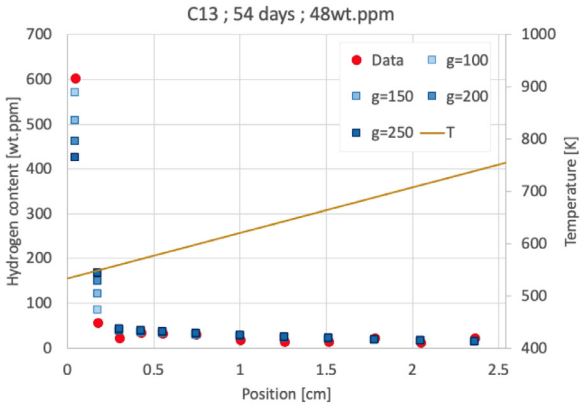

(a)

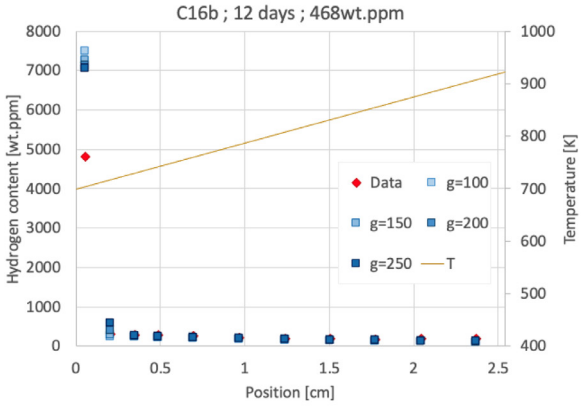

(b)

Fig. 8. Simulations of the Kammenzind linear cases. The parameter g determines the height and thickness of the hydride peak. A lower g value brings the mHNGD model closer to the initial HNGD model, in which all hydrides are concentrated in a single node of the simulation mesh. The higher g is, the broader -and lower- the hydride peak is. The parameters δ and τ have no significant impact on the results.

tice a secondary hydride peak close to the left interface, which corresponds to experimental measurements. The modified HNGD model thus captures physical behavior that the initial HNGD model did not, while providing and overall similar quality of fit. Fig. 7b shows that the formation of this secondary hydride peak is impacted by values of τ that are comparable to the duration of the annealing ($\approx 3.5 \times 10^6$ s). It has, however, no impact on the range $10^4 - 10^6$ s. If τ is set to a value significantly higher than the annealing duration (10^7 s in Fig. 7b), it restores the definition of the supersolubility from the initial HNGD model (i.e. no decrease of the effective supersolubility during the annealing), and the secondary peak does not form at all. The parameter δ has no impact on this simulation because the hydride content is too low.

4.3. Linear temperature cases

Fig. 8 shows the simulations of two of Kammenzind's linear cases [7,8]. In the same manner as in the asymmetrical cases exemplified in Fig. 5, the mHNGD model is able to accurately predict the thickness of the experimentally measured hydride rim, which was not the case with the initial HNGD model. In this case also, the value of the parameter g determines the height and thickness of the hydride peak that forms at the cold interface. The parameter δ has no significant impact on these simulations because the hydride content is too low.

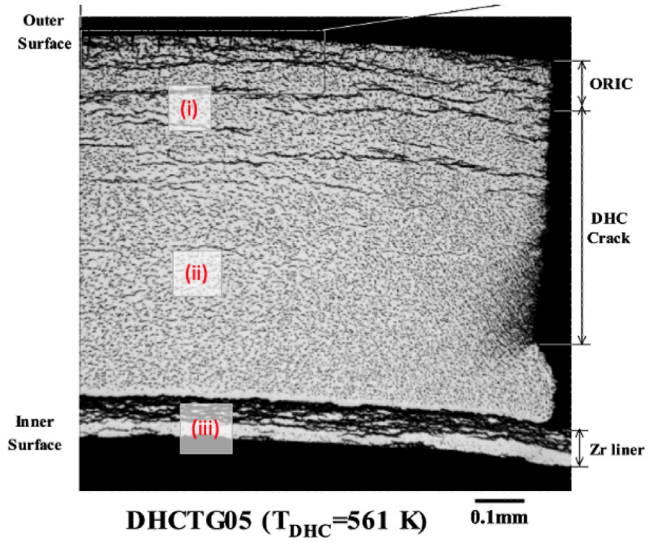

Fig. 9. Optical microscope picture of a cladding tube containing 352 wt.ppm of hydrogen, and subjected to a temperature gradient (561 – 621K) [9]. There is a zirconium liner at the inner surface of the tube. Hydrides form at the cold interface (i), and on the outer part of the inner liner (iii). A hydride-depleted region (ii) separates these two hydrided regions.

The entire set of linear cases in which precipitation occurs was used to optimize the parameter g. To quantify the quality of each simulation, we compute the correlation coefficient R^2 of the scatter (X = experimental data; Y = simulation). Doing so on a range of values gives R^2 as a function of g. For each linear case "i" the optimum value g_i is the value of g that gives the highest correlation coefficient. The spread around g_i is noted Δg_i. Once the optimum value and its uncertainty ($g_i, \Delta g_i$) are determined for each case, the overall optimum and uncertainty can be computed as a weighted average and standard deviation as defined in [13]:

$$g = \frac{\sum_{i=1}^{N} \frac{g_i^{opti}}{(\Delta g^i)^2}}{\sum_{i=1}^{N} \frac{1}{(\Delta g_i)^2}} \qquad \Delta g = \sqrt{\frac{1}{\sum_{i=1}^{N} \frac{1}{(\Delta g_i)^2}}}. \tag{12}$$

This method gives $g = 120 \pm 30$ wt.ppm. The results of the simulations for Sawatzky's and Kammenzind's experiments are gathered in the Mendeley data associated with this work, available online [14]. Out of the 22 cases, only 3 have a correlation coefficient below 0.90. All of these simulations used the same parameters: the default parameters of the initial HNGD model ([2–4]), and the newly determined mHNGD parameters: $\tau = 10^4$ s, $\delta = 1.05$, and $g = 120$ wt.ppm.

4.4. Zircaloy cladding with inner liner

In this section, we demonstrate the capability of Bison to simulate the hydride distribution in a Zircaloy nuclear cladding with a zirconium inner liner. In a previous study, cold-worked cladding tubes with a liner were charged with hydrogen and placed under a radial temperature gradient [9]. The primary goal of the study was to study delayed hydride cracking, so a hoop stress (200 to 300 MPa) was applied to the tube by placing them in a pressure vessel. Although the applied stress is not taken into account by the mHNGD model, it is interesting to see how the mHNGD model predicts the hydride distribution in the presence of a liner. Fig. 9 shows an optical microscope picture taken after exposing the tube to a temperature gradient and hoop stress. Three regions can be defined: (i) an hydrided region at the cold interface, (ii) a hydride depleted region, and (iii) the zirconium liner, with hydrides on its colder side.

Table 1
Inner liner simulation parameters [15,16].

	Zircaloy	Zirconium
TSS_D^0 (wt.ppm)	14.3×10^3	14.1×10^3
Q_D (J/mol)	36.7×10^3	38.1×10^3
TSS_P^0 (wt.ppm)	32.7×10^3	33.9×10^3
Q_P (J/mol)	25.0×10^3	27.3×10^3

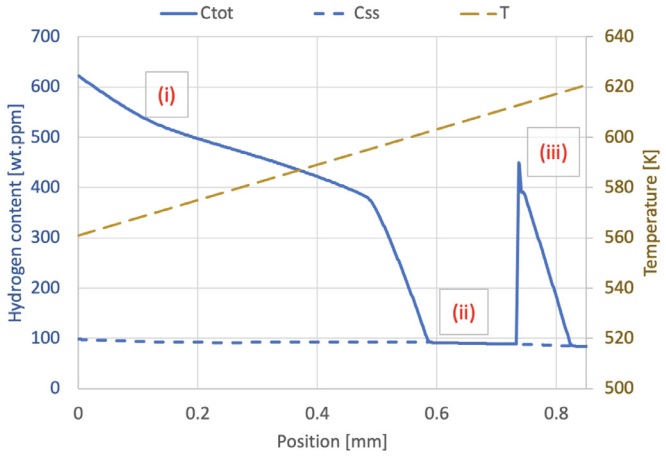

Fig. 10. mHNGD simulation of a Zircaloy cladding with inner liner under a temperature gradient (brown). The total hydrogen concentration is given by the plain blue line, and the concentration in solid solution by the dashed line. The profile presents the same main features as the experiment: (i) a hydrided region at the cold interface, (ii) a hydride-depleted region, and (iii) a hydride peak on the cold side of the inner liner. (For interpretation of the references to colour in this figure legend, the reader is referred to the web version of this article.)

To model this type of sample, we use the Bison mesh generation capabilities to create a mesh separated into two blocks (one for the cladding, and one for the liner). The mHNGD model can then be applied in each block with potentially different parameters. Une et al. showed that Zircaloy-2 and pure zirconium have significantly different solubility (TSS_D) and supersolubility (TSS_P) [15,16]. Table 1 summarizes the coefficients for the Arrhenius fits of these two parameters, using Eq. 13.

$$TSS_i = TSS_{i0} exp\left(\frac{-Q_i}{RT}\right), \tag{13}$$

where TSS_i^0 and Q_i are the preexponential factor and activation energy for the hydrogen solubility ($i = D$) and supersolubility ($i = P$). In the simulation, the sample is initially at room temperature with a uniform distribution of hydrogen. The temperature increases and reaches the annealing gradient (shown in Fig. 10) after an hour. The end of the simulation is reached after an additional 1.5 hours. Fig. 10 shows a snapshot of the final hydrogen profile taken right before the sample is cooled down to be measured. Ending the simulation at this point makes it possible to visualize the partition of hydrogen between hydrides and solid solution and their distributions in the sample while at temperature. The total hydrogen concentration is given by the plain line, and the solid solution by the dashed line. Comparing Figs. 9 and 10 shows that, even without taking stress diffusion into account, the mHNGD model accurately predicts the main features of the hydride distribution seen in Fig. 9: (i) the waterside hydrided region, (ii) a hydride-depleted region, and (iii) the liner hydrides, concentrated on the colder side of the liner.

Similar to Sawatzky's experiments in Section 4.2, in this experiment the system is not at steady state. As a result, the mH-

NGD model and the initial version give, as expected, similar results. However, if the simulation is run until steady state is reached, all hydrides end up concentrated in a single node with the initial HNGD model, which is unphysical. This is not the case with the modified version.

4.5. In-reactor scenario

The previous example features a validation of the mHNGD in an out-of-pile configuration. The mHNGD model is also able to model hydrogen behavior in an in-pile situation, as was demonstrated in the example case `spent_fuel/full_life_cycle_coarse` in Bison. In this example case featuring a stack of 10 fuel pellets, the complete life of a fuel element is simulated from irradiation (3 years) to pool storage (3 years), and dry storage (5 years). This example case is available to all Bison users. However, additional experimental data is required to validate the hydrogen distribution calculated by the mHNGD model in this configuration.

5. Testing the hypotheses

As mentioned at the beginning of Section 3, the hypotheses presented in this work are mostly based on mathematical considerations and on observations made over a large number of simulation runs. Although the changes engendered by these hypotheses were validated in Section 4 the next logical step is to further test these hypotheses physically. In this Section, we discuss some ideas and challenges associated with this goal.

5.1. Experiments

5.1.1. Supersolubility

We first focus on trying to design an experiment that could confirm the supersolubility hypothesis. In this potential experiment, a Zircaloy sample is uniformly loaded with hydrogen. Sample homogeneity can be ensured after the loading step by subjecting the sample to a temperature high enough to dissolve all hydrides and for a long enough time for the hydrogen to homogenize. The duration of such temperature hold can be determined based on the diffusion coefficient of hydrogen in zirconium. The sample should be large enough so that a piece can be cut to measure the global hydrogen content H_{tot}, while the rest of the sample is used for the following measurement.

The sample would be brought to high temperature to dissolve all hydride particles, and then be cooled down until reaching a temperature chosen so that the global hydrogen content is below the supersolubility (TSS_P) but above the solubility (TSS_D). The concentration of hydrogen in solid solution and the hydride content can be recorded *in-situ* during the experiment using X-ray diffraction as was done for Lacroix's thermal transients benchmark ([2,3]). This makes it possible to obtain a value for τ.

Fig. 11 shows a simulation of the heat treatment for a Zircaloy sample containing 200 wt.ppm of hydrogen. The temperature is given by the dashed brown line, the supersolubility is shown in green, the concentration of hydrogen in solid solution in blue, and the solubility in dotted green. First the sample is brought to a temperature high enough to dissolve all hydrides, then brought down to the previously chosen annealing temperature. The annealing starts at $t = t_0$. If the hypothesis is true, nucleation will occur when the effective supersolubility reaches the hydrogen content of the sample, at $t = t_1$, i.e $TSS_P^{eff}(t_1) = H_{tot}$. As per Eq. 5, the parameter τ is then given by

$$\tau = \frac{t_1 - t_0}{ln\left(\frac{TSS_P - TSS_D^{eff}}{H_{tot} - TSS_D^{eff}}\right)}. \quad (14)$$

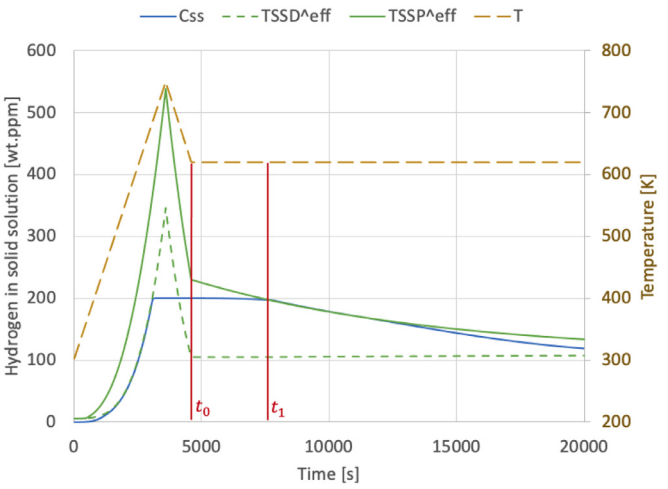

Fig. 11. Simulation of an experiment designed to determine the parameter τ, showing the temperature (brown dashed), the effective supersolubility (green), the effective solubility (green dotted), and the hydrogen concentration (blue). Once all hydrides are dissolved, τ can be determined using the time elapsed between the start of the annealing t_0 and the start of precipitation t_1. This simulation uses the parameters $\tau = 10^4$ s, $\delta = 1.05$, and $g = 120$ wt.ppm. (For interpretation of the references to colour in this figure legend, the reader is referred to the web version of this article.)

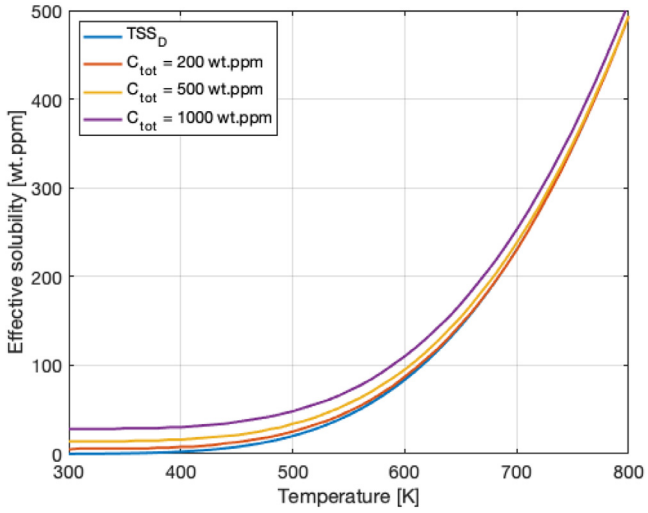

Fig. 12. Effective solubility as a function of temperature for different total hydrogen content. The difference in solubility in the hypothesis is of the order of the typical experimental uncertainties on hydrogen content measurements.

The blue curve (C_{ss}) shows what would be recorded during the experiment. First all hydrides dissolve during the heat-up, causing an increase of the concentration of hydrogen in solution. Nothing would happen during the cool down, C_{ss} remains constant. Then, at some point the concentration in solid solution would start decreasing again when the nucleation barrier is sufficiently low. The time elapsed between the beginning of the temperature hold and the start of precipitation gives a value for τ, as per Eq. 14.

5.1.2. Solubility

Testing the hypothesis of increased solubility with increasing hydride content appears to be particularly challenging, for its effect is quite subtle. Fig. 12 shows the effective solubility in a uniform sample, as a function of temperature for different total hydrogen contents. As expected, the difference of solubility is maximum at low temperatures, i.e. when the hydride content is at its highest. However, even at room temperature the difference of

solubility between a sample without hydrides and one containing over 950 wt.ppm of hydrides is only about 20 wt.ppm when using $g = 120$ wt.ppm. Unfortunately, such a small difference in hydride content is close to experimental uncertainties. A better approach could be to use lower scale simulation tools, such as phase-field modeling or density functional theory, to test this hypothesis.

5.2. Lower scale simulations

Lower scale simulations could potentially show that the solubility of hydrogen in zirconium depends on the hydride content. The physical basis for this hypothesis is, as described above, that when hydrides precipitate, they deform the neighboring matrix elastically and/or plastically, both of which could increase the hydrogen solubility of the material. For example, Density Functional Theory (DFT) calculations could be used to study the effect of dislocations in the zirconium matrix on the solubility. Also, a quantitative phase field model of zirconium hydrides that includes plasticity could evaluate how the hydride content affects the solubility. Such studies could provide insight on the mechanisms at play in the hydrogen solubility increase.

6. Conclusion

The development of a simulation tool capable of more precisely predicting the formation of hydrides can contribute to the safe operation of nuclear fuel in reactor and its safe long term storage. The present work improves the existing HNGD model, including in predicting the steady state hydride distribution under a temperature gradient. The origin of the unphysical behavior was identified as a hydride instability when both Fick and Soret components of the hydrogen flux go in the same direction and was addressed by hypothesizing that (i) the hydride precipitation nucleation threshold decreases during long anneals compared to short anneals, and (ii) the hydrogen solubility increases when hydride particles precipitate. These hypotheses were implemented into the INL nuclear fuel performance code Bison and the predictions of the model were validated against experimental measurements. The modified HNGD model predicts more accurately the thickness of the hydrided region that forms at the cold interface of the samples, and in general provides a more precise simulation of the hydrogen profile during thermal treatment. The modified model also predicts some phenomena previously missing, such as the formation of a secondary hydride peak during Sawatzky's experiments. In addition, the Bison capability to simulate hydride distribution in a Zircaloy cladding with an inner zirconium liner was demonstrated. Finally, the possibilities and challenges of testing the hypotheses with experiments and lower scale simulations were discussed. The modified HNGD model is available on a public Github repository.

Data availability

The modified HNGD model is available on a public Github repository [8]. The data and Matlab scripts to reproduce the plots for Sawatzky's and Kammenzind's experiments are available on a Mendeley Data repository [14].

Declaration of Competing Interest

The authors declare that they have no known competing financial interests or personal relationships that could have appeared to influence the work reported in this paper.

CRediT authorship contribution statement

Florian Passelaigue: Conceptualization, Methodology, Software, Writing – original draft, Visualization. **Pierre-Clément A. Simon:** Conceptualization, Software, Validation, Writing – review & editing. **Arthur T. Motta:** Supervision, Conceptualization, Validation, Writing – review & editing, Funding acquisition.

Acknowlgedgments

This work was performed with the support of the DOE NEUP IRP-17-13708 project "Development of a Mechanistic Hydride Behavior Model for Spent Fuel Cladding Storage and Transportation"; we acknowledge helpful discussions with the other members of the IRP project. In particular, we acknowledge the help of Bruce Kammenzind, who produced the majority of the data used in this work, and provided valuable insights when discussing the hypotheses presented here. We also acknowledge Dr. Quentin Auzoux of the CEA-Saclay for his help with finding data on cladding with inner liner.

Appendix A. Analytical steady state derivation

In this Appendix we derive the analytical solution for the steady state of a linear Zircaloy sample subjected to a constant temperature profile. This temperature profile is not necessarily linear, however we assume that the lowest temperature is $T_0 \equiv T(x = 0)$. Several steps are needed to reach the solution for the hydride distribution C_{Prec}, and each step builds on the previous one: (Appendix A.1) determines the steady state equation for hydrogen distribution in the two-phase region, (Appendix A.2) derives the polynomial p (Eq. 6) as a function of x, (Appendix A.3) derives the hydride volume fraction as a function of x, and (Appendix A.4) derives the hydride content C_{Prec} as a function of x. We also derive the profile of hydrogen in solid solution (Appendix A.5). Combining both solutions provides with a complete solution for the steady state of the system.

A1. Steady state equation

At steady state and in assuming one dimensional diffusion, the equation system for the evolution of C_{Prec} and C_{ss} given in Eq. 2 can be written as

$$\begin{cases} \dfrac{\partial C_{Prec}}{\partial t} = 0 \\ \dfrac{\partial C_{ss}}{\partial t} = 0 = \dfrac{\partial J}{\partial x} \end{cases}. \tag{A.1}$$

The "no precipitation nor dissolution" condition (first line) is fulfilled if and only if the concentration of hydrogen in solid solution is equal to the solubility TSS_D^{eff}. The condition $\frac{\partial J}{\partial x} = 0$ means that the hydrogen flux is uniform, and there is a no-flux boundary condition at the end of the sample, i.e. $J(0) = 0$, so the flux must be null at all positions at steady state. This yields the steady state equation:

$$\left.\begin{array}{l} C_{ss} = TSS_D^{eff} \\ J = 0 \end{array}\right\} \Rightarrow \frac{dTSS_D^{eff}}{dx} = \frac{-Q^* TSS_D^{eff}}{RT^2}\frac{dT}{dx}. \tag{A.2}$$

A2. Analytical solution for p

Let p be a function such that the effective solubility is given by

$$TSS_D^{eff}(x) = TSS_D(T(x)) + p(x). \tag{A.3}$$

The solubility derivative is then given by

$$\frac{\partial TSS_D^{eff}}{\partial x} = \frac{Q_D}{RT^2}\frac{dT}{dx}TSS_D + \frac{\partial p}{\partial x}, \tag{A.4}$$

with Q_D the activation energy for TSS_D (Eq. 13) and the steady state Eq. A.2 becomes

$$\frac{\partial p}{\partial x} + \frac{Q^*}{RT^2}p = -\frac{Q^* + Q_D}{RT^2}\frac{dT}{dx}TSS_D. \tag{A.5}$$

p can be written as $p(x) = p_0(x) \times u(x)$ where p_0 and u obey the following system of equations:

$$\begin{cases} \frac{dp_0}{dx} + \frac{Q^*}{RT^2}p_0 = 0 \\ \frac{du}{dx}p_0 = \frac{-Q^* - Q_D}{RT^2}\frac{dT}{dx}TSS_D \end{cases}. \tag{A.6}$$

The first equation is separable:

$$\begin{aligned} &\frac{1}{p_0}\frac{dp_0}{dx} = \frac{-Q^*}{R}\frac{1}{T}\frac{dT}{dx} \\ &\Rightarrow \left[ln(p_0)\right]^x = \frac{-Q^*}{R}\left[\frac{-1}{T}\right]^x, \end{aligned} \tag{A.7}$$

so a suitable function is:

$$p_0(x) = exp\left(\frac{Q^*}{RT(x)}\right). \tag{A.8}$$

Introducing p_0 in the second equation of Eq. A.6 yields

$$\frac{du}{dx} = TSS_D^0\frac{-Q^* - Q_D}{RT^2}\frac{dT}{dx}exp\left(\frac{-Q^* - Q_D}{RT}\right) \tag{A.9}$$

Integrating each side of Eq. A.9 gives:

$$\begin{aligned} &u(x) - u(0) = TSS_D^0\left[-exp\left(\frac{-Q^* - Q_D}{RT}\right)\right]_0^x \\ &= TSS_D(T_0)exp\left(\frac{-Q^*}{RT_0}\right) - TSS_D(T)exp\left(\frac{-Q^*}{RT}\right) \end{aligned} \tag{A.10}$$

Combining p_0 and u gives

$$\begin{aligned} &p = Kexp\left(\frac{Q^*}{RT}\right) - TSS_D(T) + \\ &TSS_D(T_0)exp\left(\frac{Q^*}{R}\left(\frac{1}{T} - \frac{1}{T_0}\right)\right) \end{aligned}. \tag{A.11}$$

The integration constant $K \equiv u(0)$ can be determined using mass conservation, and $T_0 \equiv T(0)$ is the cold temperature.

A3. Analytical solution for v_δ

Let us recall the modifying polynomial given by Eq. 11 :

$$p(v_\delta) = gv_\delta - \left((1-\delta)TSS_D + g\right)v_\delta^2. \tag{A.12}$$

The hydride volume fraction as a function of x can then be derived as follows:

$$p = av_\delta^2 + bv_\delta \Leftrightarrow v_\delta^2 + \frac{b}{a}v_\delta = \frac{p}{a} \tag{A.13}$$

$$\Leftrightarrow v_\delta^2 + \frac{b}{a}v_\delta + \frac{b}{2a} = \frac{p}{a} + \frac{b}{2a} \tag{A.14}$$

$$\Leftrightarrow \left(v_\delta + \frac{b}{2a}\right)^2 = \frac{2p+b}{a} \tag{A.15}$$

$$\Leftrightarrow v_\delta(x) = \frac{-b}{2a} \pm \sqrt{\frac{2p(x)+b}{a}} \tag{A.16}$$

Because physically v_δ decreases when T increases, and because we assume that the cold temperature is at $x = 0$, only the $(-)$ solution is acceptable, so we finally obtain

$$\begin{aligned} &v_\delta(x) = \frac{g}{2\left((1-\delta)TSS_D(x) + g\right)} - \\ &\sqrt{\frac{2p(x)+g}{\left((1-\delta)TSS_D(x) + g\right)}} \end{aligned}. \tag{A.17}$$

A4. Analytical solution for C_{Prec}

The hydride volume fraction is a function of the hydride content C_{Prec} (Eq. 7):

$$v_\delta = \frac{1}{x_\delta - x_{TSSD}} \times \frac{C_{Prec}}{C_{tot}\left(1 - \frac{M_H}{M_{Zr}}\right) + 10^6\frac{M_H}{M_{Zr}}}, \tag{A.18}$$

At steady state the concentration of hydrogen in solid solution is equal to the solubility, i.e. $C_{ss} = TSS_D^{eff}$, so Eq. A.18 can be written as

$$\begin{aligned} &C_{Prec} = v_\delta(x)(x_\delta - x_{TSSD}) \times \\ &\left[\left(C_{Prec} + TSS_D^{eff}\right)\left(1 - \frac{M_H}{M_{Zr}}\right) + 10^6\frac{M_H}{M_{Zr}}\right] \end{aligned} \tag{A.19}$$

Developing TSS_D^{eff} and solving for C_{Prec} finally gives

$$\begin{aligned} &C_{Prec}(x) = TSS_D v_\delta(x)(x_\delta - x_{TSSD}) \times \\ &\frac{\left(1 + \frac{p(x)}{TSS_D}\right)\left(1 - \frac{M_H}{M_{Zr}}\right) + \frac{10^6}{TSS_D}\frac{M_H}{M_{Zr}}}{1 - v_\delta(x)(x_\delta - x_{TSSD})\left(1 - \frac{M_H}{M_{Zr}}\right)} \end{aligned}. \tag{A.20}$$

A5. Analytical solution for C_{ss}

The analytical solution for the distribution of hydrogen in solid solution is derived from the no-flux condition shown in Section A.1:

$$\frac{dC_{ss}}{dx} = -\frac{Q^* C_{ss}}{RT^2}\frac{dT}{dx} \tag{A.21}$$

$$\frac{1}{C_{ss}}\frac{dC_{ss}}{dx} = -\frac{Q^*}{R}\frac{1}{T^2}\frac{dT}{dx} \tag{A.22}$$

$$\int_0^x \frac{C'_{ss}(u)}{C_{ss}(u)}du = -\frac{Q^*}{R}\int_0^x \frac{T'(u)}{T(u)^2}du \tag{A.23}$$

$$\left[ln\left(C_{ss}(u)\right)\right]_0^x = -\frac{Q^*}{R}\left[-\frac{1}{T(u)}\right]_0^x \tag{A.24}$$

$$ln\frac{C_{ss}(x)}{C_{ss}(0)} = -\frac{Q^*}{R}\left(-\frac{1}{T(x)} + \frac{1}{T(0)}\right) \tag{A.25}$$

$$C_{ss}(x) = C_{ss}(0)exp\left(\frac{Q^*}{R}\left(\frac{1}{T(x)} - \frac{1}{T_0}\right)\right) \tag{A.26}$$

Combining Eq. A.20 and A.26 gives the total hydrogen distribution at steady state. In this paper it was used to estimate g by comparing the analytical results with the experimental data. The Mendeley data associated with this paper includes a Matlab script to build such an analytical solution [14].

References

[1] A.T. Motta, L. Capolungo, L.-Q. Chen, M.N. Cinbiz, M.R. Daymond, D.A. Koss, E. Lacroix, G. Pastore, P.-C.A. Simon, M.R. Tonks, B.D. Wirth, M.A. Zikry, Hydrogen in zirconium alloys: a review, J. Nucl. Mater. 518 (2019) pp440–460, doi:10.1016/J.JNUCMAT.2019.02.042.

[2] E. Lacroix, P.-C.A. Simon, A.T. Motta, J. Almer, Zirconium hydride precipitation and dissolution kinetics in zirconium alloys, Zirconium in the Nuclear Industry: 19th International Symposium, STP 1622 (2019) 67–91.

[3] E. Lacroix, Modeling zirconium hydride precipitation and dissolution in zirconium alloys, Ph.D. in Nuclear Engineering, The Pennsylvania State University (2019).

[4] F. Passelaigue, E. Lacroix, G. Pastore, A.T. Motta, Implementation and validation of the hydride nucleation-Growth-Dissolution (HNGD) model in Bison, J. Nucl. Mater. 544 (2021).

[5] R. Williamson, J. Hales, S. Novascone, G. Pastore, K. Gamble, B. Spencer, W. Jiang, S. Pitts, A. Casagranda, D. Schwen, A. Zabriskie, A. Toptan, R. Gardner, C. Matthews, W. Liu, H. Chen, Bison: a flexible code for advanced simulation of the performance of multiple nuclear fuel forms, Nucl. Technol. 207 (7) (2021) 954–980, doi:10.1080/00295450.2020.1836940.

[6] A. Sawatzky, Hydrogen in zircaloy-2: its distribution and heat of transport, J. Nucl. Mater. 2 (1960) 321–328, doi:10.1016/0022-3115(60)90004-0.
[7] J. Merlino, Experiments in hydrogen distribution in thermal gradients calculated using bison, M.Eng. paper in Nuclear Engineering, The Pennsylvania State University (2019).
[8] F. Passelaigue, Github repository for a C++ implementation of the HNGD model, 2021 https://github.com/FloPasselaigue/HNGD.
[9] K. Sakamoto, M. Nakatsuka, T. Higuchi, K. Ito, Role of radial temperature gradient in outside-in type failure of high burn-up fuel cladding tubes during power ramp tests, Proceedings of the Water Reactor Fuel Performance Meeting - WRFPM / Top Fuel 2009 (2009) 268–275.
[10] K. Kelton, A. Greer, Nucleation in Condensed Matter, Pergamon, 2010.
[11] P.-C. Simon, L.K. Aagesen, A.M. Jokisaari, L.-Q. Chen, M.R. Daymond, A.T. Motta, M.R. Tonks, Investigation of δ zirconium hydride morphology in a single crystal using quantitative phase field simulations supported by experiments, J. Nucl. Mater. 557 (2021) 153303, doi:10.1016/j.jnucmat.2021.153303.
[12] Z. Zhao, M. Blat-Yrieix, J.P. Morniroli, A. Legris, L. Thuinet, Y. Kihn, A. Ambard, L. Legras, Characterization of zirconium hydrides and phase field approach to a mesoscopic-Scale modeling of their precipitation, Zirconium in the Nuclear Industry: 15th International Symposium STP 1505 (2009) 29–48, doi:10.1520/STP48129S.
[13] P. Bevington, D. Robinson, Data Reduction and Error Analysis for the Physical Sciences, 3rd edition, McGraw-Hill Education, 2003.
[14] F. Passelaigue, P.-C. A. Simon, A.T. Motta, "Modified_HNGD_Validation", Mendeley Data, v1, https://dx.doi.org/10.17632/6ftsfyfpbz.1.
[15] K. Une, S. Ishimoto, Terminal solid solubility of hydrogen in unalloyed zirconium by differential scanning calorimetry, J. Nucl. Sci. Technol. 41 (2004) 949–952, doi:10.1080/18811248.2004.9715569.
[16] K. Une, S. Ishimoto, Y. Etoh, K. Ito, K. Ogata, T. Baba, K. Kamimura, Y. Kobayashi, The terminal solid solubility of hydrogen in irradiated zircaloy-2 and microscopic modeling of hydride behavior, J. Nucl. Mater. 389 (2009) 127–136, doi:10.1016/j.jnucmat.2009.01.017.